New evidence for surface water ice in small-scale cold traps and in three large craters at the north polar region of Mercury from the Mercury Laser Altimeter

Ariel N. Deutsch[1], Gregory A. Neumann[2], and James W. Head[1]

[1]Department of Earth, Environmental and Planetary Sciences, Brown University, Providence, RI 02912, USA

[2]NASA Goddard Space Flight Center, Greenbelt, MD 20771, USA

Corresponding author: Ariel Deutsch (ariel_deutsch@brown.edu)

Key Points:

- Typical polar water-ice deposits are veneered; we find three new craters with high surface reflectances indicative of exposed ice
- We also identify clusters of enhanced surface reflectance indicative of small-scale cold traps with diameters < 5 km
- We suggest that a substantial amount of Mercury's water ice exists within micro-cold traps, within rough patches and inter-crater terrain

Abstract

The Mercury Laser Altimeter (MLA) measured surface reflectance, r_s, at 1064 nm. On Mercury, most water-ice deposits have anomalously low r_s values indicative of an insulating layer beneath which ice is buried. Previous detections of surface water ice (without an insulating layer) were limited to seven craters. Here we map r_s in three additional permanently shadowed craters that host radar-bright deposits. Each crater has a mean r_s value > 0.3, suggesting that water ice is exposed at the surface without an overlying insulating layer, bringing the total to ten large craters that host exposed water ice at Mercury's north pole. We also identify small-scale cold traps (< 5 km) where r_s > 0.3 and permanent shadows have biannual maximum surface temperatures < 100 K. We suggest that a substantial amount of Mercury's water ice is not confined to large craters, but exists within micro-cold traps, within rough patches and inter-crater terrain.

1 Introduction

Both Earth-based and spacecraft observations provide evidence that Mercury hosts water ice within its permanently shadowed regions (PSRs) near the poles. Earth-based radar images of Mercury first revealed highly reflective materials that are consistent with water ice [*Slade et al*., 1992; *Harmon and Slade*, 1992; *Butler et al*., 1993; *Harmon et al*., 1994, 2001, 2011]. These "radar-bright" materials collocate with PSRs derived from images and topography [*Chabot et al*., 2012, 2013; *Deutsch et al*., 2016]. Thermal models derived from topography indicate that PSRs are stable environments for near-surface and sometimes surface water ice on geologic timescales [*Paige et al*., 2013]. Furthermore, enhanced concentrations of hydrogen have been detected in the north polar region [*Lawrence et al*., 2013].

The Mercury Laser Altimeter (MLA) instrument onboard the MErcury Surface, Space ENvironment, GEochemistry, and Ranging (MESSENGER) spacecraft measured the surface reflectance at 1064 nm at zero phase angle across the northern hemisphere of Mercury. The surface reflectance within PSRs is anomalously higher or lower than the average reflectance of Mercury [*Neumann et al*., 2013]. Reflectance anomalies correlate with areas that thermal models predict are environments capable of hosting stable water ice [*Paige et al*., 2013]. On Mercury, these environments are always PSRs [*Paige et al*., 2013], however not all PSRs are necessarily occupied cold-traps [*Deutsch et al*., 2016; *Chabot et al*., 2017]. Typically, water-ice deposits on Mercury are insulated by a layer of low-reflectance materials, which is estimated to be 10–30 cm thick on the basis of comparative variation of the flux of epithermal and fast neutrons with latitude [*Lawrence et al*., 2013]. Low-reflectance surfaces are interpreted to be composed of volatile species other than water and are found where water ice is predicted to be stable only in the near subsurface [*Paige et al*., 2013]. These insulating low-reflectance deposits have been suggested to be composed of organic-rich compounds such as those found in comets and primitive meteorites [*Zhang and Paige*, 2009; 2010; *Paige et al*, 2013].

In contrast to low-reflectance deposits, which are suggestive of subsurface ice, high-reflectance deposits are indicative of surface water ice [*Neumann et al*., 2013]. MLA reflectance [*Neumann et al*., 2013] and MDIS-scattered-light imaging [*Chabot et al*., 2014] observations revealed one such high-reflectance surface on the floor of Prokofiev crater (85.8°N, 62.9°E). The anomalously high-reflectance deposit collocates with radar-bright material [*Harmon et al*., 2011]. Thermal models [*Paige et al*., 2013] indicate that the floors of some higher-latitude craters, including Prokofiev, can support water ice exposed at the surface for billions of years without the need for an insulating layer. Here we have investigated these craters using newly calibrated MLA reflectance data [*Neumann et al*., 2017].

Recent work reported on the surface reflectances near Mercury's north pole and showed a steady increase in reflectance from 85.3°N to 90°N [*Neumann et al*., 2017]. While the extensive ice deposit exposed at Prokofiev contributes to an increase in reflectance from ~85°N to the pole, this increasing trend of reflectance remained even when the contribution of 120 permanently shadowed craters with diameters between 7 and 120 km was masked [*Neumann et al*., 2017]. This trend suggests that there are surface water-ice deposits in micro-cold traps, below the scale of 7 km, that are concentrated northward of ~85°N [*Neumann et al*., 2017].

Thermal illumination models further corroborate the hypothesis that micro-cold traps may host water-ice deposits on the surface of Mercury. Recent thermal models [*Rubanenko et al*., 2017] linked surface reflectance and ice stability and suggested that a large fraction of water-ice deposits exist inside micro-cold traps (of scales 10–100 m) distributed along the inter-crater terrain, in areas that are smaller than the MESSENGER spatial scale [*Rubanenko et al*., 2017].

Earlier work [*Paige et al*., 2014] examined the correlation between MLA reflectance and annual average subsurface temperatures, T_{avg}, for the region from 75°N to 84°N. This work was completed after two years of MESSENGER operations, and thus was limited to latitudes southward of 84°N due to the inclination of the spacecraft orbit. From 75°N to 84°N, there was a poleward darkening in the MLA reflectance map and a linear increase in reflectance with temperature in the range 100 K < T_{avg} < 290 K [*Paige et al*., 2014]. *Paige et al*. [2014] suggested that the presence of dark surface material marks the locations of small-scale volatile cold traps that are mixed at spatial scales below those that can be resolved by MLA and Earth-based radar measurements. Modeling the total surficial cold trap areas suggests that 22% of the surface poleward of 70°N is covered by low-reflectance material in micro-cold traps, while only 4% of the surface area poleward of 70°N is covered by low-reflectance material at spatial scales of > 0.5 km [*Paige et al*., 2014], indicating that micro-cold traps sequester a substantial proportion of the total cold-trapped volatiles at Mercury's near-subsurface.

Given that surface reflectance increases northward of ~85°N [*Neumann et al*., 2017] and that micro-cold traps may be ubiquitous at latitudes northward of ~75°N [*Rubanenko et al*., 2017], we are interested in the detection of exposures of water-ice deposits present at the surface of Mercury at small spatial scales. Following the Earth-based identification of high radar-backscatter deposits in polar craters, the only detections of exposed water ice have been in large, permanently shadowed craters: Prokofiev crater [*Neumann et al*., 2013; *Chabot et al*., 2014], as well as limited off-nadir MLA measurements of A, C, D2, Kandinsky, i5, and Y craters [*Neumann et al*., 2013] (For craters that do not have formal IAU names, we adopt informal nomenclature from published maps). Here we investigate the presence of specific small-scale cold traps by searching for clustered MLA-measured surface reflectance, r_s, enhancements at 1064-nm wavelength that can be observed at the resolution of MLA footprints. We compare the distribution of r_s enhancements to that of Earth-based radar data [*Harmon et al*., 2011], areas of permanent shadow [*Deutsch et al*., 2016], and biannual maximum surface temperatures, T_{max}, < 100 K [*Paige et al*., 2013] to discuss the implications for reservoirs of long-lived water ice exposed at the surface of Mercury inside micro-cold traps.

We also map r_s and density of energy returns in Chesterton, Tolkien, and Tryggvadóttir craters. Like Prokofiev, these three permanently shadowed craters host extensive radar-bright deposits indicative of water ice [*Harmon et al*., 2011]. However, MESSENGER only acquired limited off-nadir observations of these craters due to their proximity to the pole. The nominally calibrated r_s measurements of these craters did not show distinctive regions of r_s > 0.3 in contrast to those in Prokofiev acquired at more favorable geometry. The greater density of returns observed within the PSRs prompted a reexamination of the calibration to account for a downward bias due to highly oblique geometry [*Neumann et al*., 2017]. Utilizing the complete orbital dataset and empirically re-calibrated data, we calculate the mean r_s within the craters and outside the craters, and discuss the implications for surface water-ice deposits hosted by permanently shadowed craters close to the north pole of Mercury.

2 Methodology

2.1 Small-scale cold traps

The MESSENGER project denoted orbital mission phases "Mercury Orbit Year 1" through "Year 4", from March 2011 through March 2015. MLA operated near-continuously during these years, and intermittently during the 5th year until spacecraft impact on 30 April 2015. Periapsis altitude was maintained between 200 and 500 km during Year 1 by propulsive maneuvers. After completion of the nominal one-year mission, the elliptical orbit period was reduced from 12 to 8 hours, allowing more frequent targeted observations. The periapsis was allowed to drift above 500 km to conserve fuel during Year 2, with the latitude of periapsis increasing to a maximum of 84°N. During Years 3 and 4, the periapsis latitude declined to 60°N while periapsis altitude gradually lowered, allowing further off-nadir targeting of polar regions. Year 4 (ending 17 March 2014) and the remaining days of operation are referred to here as the "final year."

The MLA instrument illuminated areas on the surface of Mercury between 20 and 80 m in diameter at 350- to 450-m intervals [*Cavanaugh et al*., 2007]. When a reflected pulse enters the receiver, it is detected by a pair of discriminators. Its amplitude and duration are affected by surface reflectance as well as by the dispersion in time due to surface slope and roughness. The pulse energy is estimated from a simple triangular model for the pulse waveform that fits the rising and falling edges of the trigger at each threshold [*Neumann et al*. 2013]. Combined with the energy measurement of the outgoing laser pulse, an estimate of reflectance is obtained via the lidar link equation [*Sun and Neumann*, 2015].

Over the course of the orbital mission, MLA experienced a wide range of altitudes and thermal conditions, with many redundant reflectance observations at latitudes below 84°N where ground tracks all intersect. The orbital geometry and sunshade keep-in (SKI) constraint caused observations to occur at varying ranges and emission angles, leading to varying degrees of pulse dispersion. Averaging these observations over mostly uniform terrain, we have empirically corrected the changes in reflectance as a function of range and emission angle. We also corrected for an apparent decline in reflectance due to the anticipated aging of the instrument over the course of the mission.

Using publicly available data covering Mission Years 1–4, we produced a map of surface reflectance at a wavelength of 1064 nm of the north polar region from 82.5°N to 90°N at zero phase angle, producing a photometrically uniform data set (Fig. 1) [*Neumann et al*., 2017]. The newly reprocessed MLA radiometry data are available on the NASA Planetary Geodynamics Data Archive (pgda.gsfc.nasa.gov). With the empirically recalibrated map of r_s values, we searched for clusters of pulses that show reflectance enhancements, where $r_s > 0.3$, suggestive of exposed water-ice deposits. We then compared any areas that show r_s enhancements to areas with radar-bright material [*Harmon et al*., 2011], permanent shadow [*Deutsch et al*., 2016], and where $T_{max} < 100$ K [*Paige et al*., 2013], indicating the presence of exposed water ice.

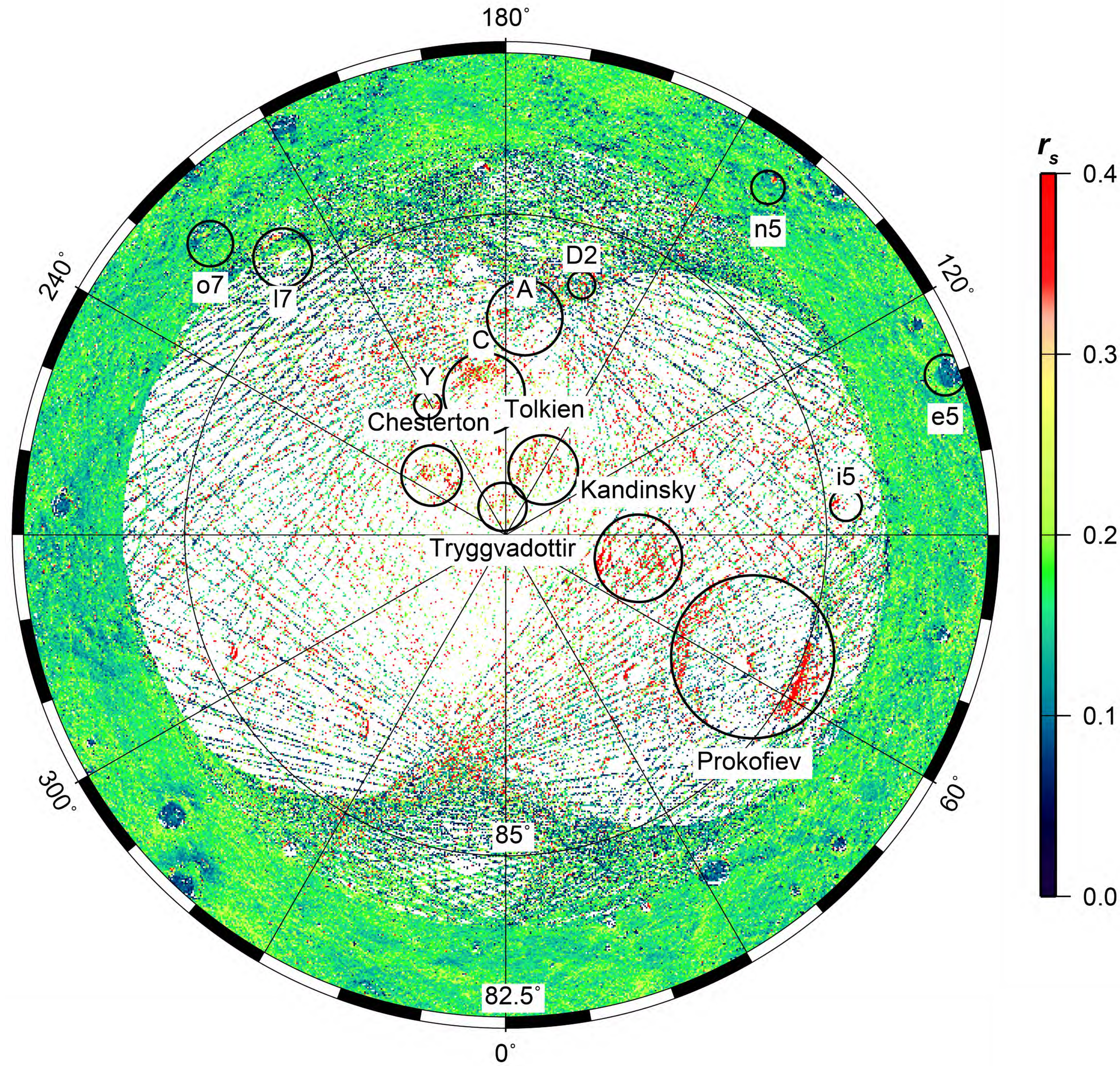

Fig. 1. MLA-derived surface reflectance, r_s, at 1064 nm from 82.5ºN to 90°N, modified from *Neumann et al.* [2017]. Large craters (Prokofiev, Chesterton, Tolkien, Tryggvadóttir, Kandinsky, C, Y, and i5) that are identified as hosting exposed water ice are labeled. Small-scale cold traps (n5, o7, e5, and l7) that are identified as hosting exposed water ice are labeled. Polar stereographic projection.

2.2 Large craters

We mapped measurements of surface reflectance, r_s, at 1064-nm in Chesterton, Tolkien, and Tryggvadóttir. We calculated the mean r_s values inside and outside each crater for a range of $2R$, where R is the radius of the crater. For each crater, we determined if there was a substantial deviation in reflectance between the crater floor and the surrounding terrain.

We also mapped the density of returns for these craters for the extent of the entire mission. The probability of detection is strongly affected by the spacecraft geometry, and specifically the phase angle. As the probability of detection increases, the energy enhancement returned by MLA typically coincides with a double return, enabling a reflectance measurement by MLA [*Sun and Neumann*, 2015]. Along a single MLA track, when viewing conditions are relatively constant, the enhanced number of returns provides a further constraint on energy returns at the high latitudes, where reflectance measurements were characteristically difficult due to ranging obliquely.

3 Results

3.1 Small-scale cold traps

After surveying the surface reflectance map (Fig. 1), we identified four clusters of MLA pulses that have values of $r_s > 0.3$. These four clusters are located in small-scale cold traps, in small yet resolvable areas that are between 2 and 5 km in diameter, in craters n5, o7, l7, and to the north of e5.

3.1.1 Small-scale cold trap in crater n5

Crater n5 has a circular topographic low located near the southeast portion of its rim, remnant of a degraded crater (Fig. 2a; white arrow). This topography nested within an already permanently shadowed crater creates a doubly shadowed cold trap. Thermal stability models predict that this local area is capable of sustaining surface ice [*Paige et al*., 2013]. Surface reflectance measurements (Fig. 2b, c) show a distinct enhancement in this topographic low in comparison to the surrounding terrain; this is observable both in MLA data collected during the low-altitude campaign completed during MESSENGER's final year of operations (Fig. 2c) and also in all of the measurements acquired up until the final year of the mission (Fig. 2b). The high r_s values coincide with PSRs [*Deutsch et al*., 2016] and radar-bright material [*Harmon et al*., 2011] using a threshold of four standard deviations of the noise (Fig. 2d).

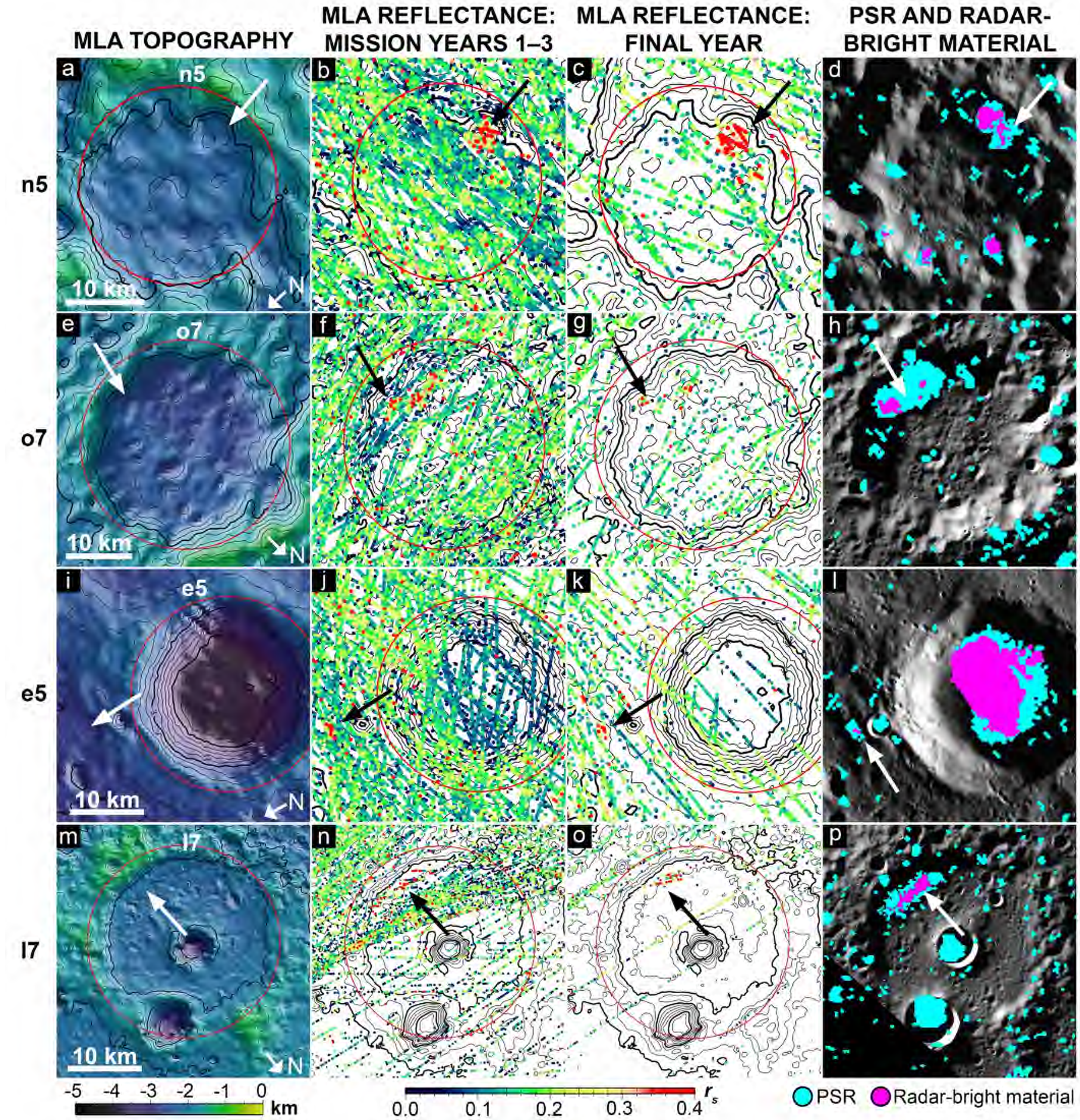

Fig. 2. Identified small-scale cold traps hosting exposed water ice. The first column shows 200-m topography contours that highlight (a) the topographic low in crater n5 (25-km diameter, centered at 83.2°N, 143.0°E), (e) the topographic low in crater o7 (32-km diameter, centered at 83.5°N, 225.4°E), (i) the ridge outside of crater e5 (26-km diameter, centered at 82.7°N, 110.0°E) and (m) the flat expanse in crater l7 (39-km diameter, 87.8°N, 188.8°E). The second column shows r_s values from years 1–3. The third column shows r_s values from only the final year of MESSENGER operations. The fourth column shows MDIS images of the surface with PSRs in blue [*Deutsch et al.*, 2016] and radar-bright materials in pink [*Harmon et al.*, 2011].

3.1.2 Small-scale cold trap in crater o7

In a manner similar to crater n5, crater o7 has a small, circular depression inside the crater at the edge of the wall (Fig. 2e; white arrow). This topographic low is positioned within the PSR of o7 (Fig. 2h) and thus provides a doubly shadowed thermal environment. This topography corresponds to regions in thermal models that are predicted to have T_{max} < 100 K, and thus capable of hosting exposed water ice [*Paige et al*., 2013]. This small-scale cold trap does not perfectly collocate with radar-bright material; however, the PSR for o7 does show evidence for a radar-bright signature (Fig. 2h), and the patchy radar-bright pixels observed in crater o7 may be due to radar-viewing limitations. Crater o7 is located near 225°E, and previous work mapping the distribution of PSRs and radar-bright material across this longitude showed that there is substantial permanent shadow that lacks radar-bright deposits [*Deutsch et al*., 2016]. *Deutsch et al*. [2016] suggested that limitations in the radar viewing geometry and sensitivity may be skewing the radar data in this region or that thicker lag deposits may attenuate the radar signature. Here, the thermal and reflectance data are indicative of a small-scale cold trap with exposed water ice; there is a strong correlation between where the thermal models predict a sharp decrease in temperature and where MLA observes a sharp increase in r_s values (shaded box in Fig. 3).

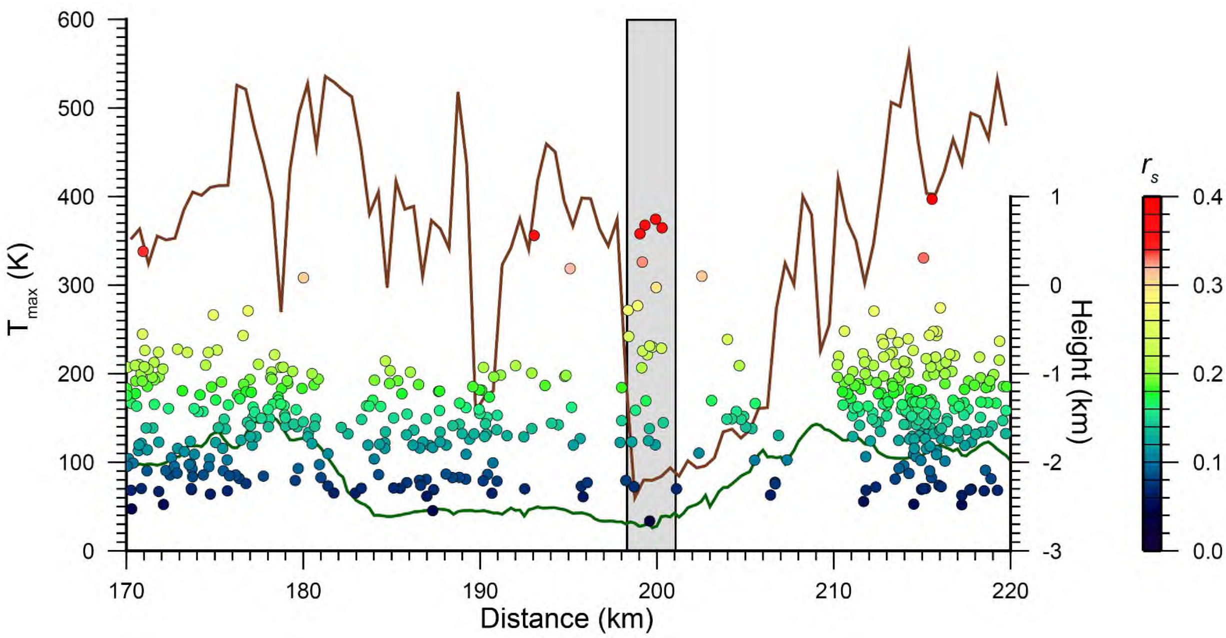

Fig. 3. Small-scale cold trap at crater o7. Green line shows the topography of host crater o7 (32-km diameter). Colored circles represent individual surface reflectance, r_s, pulses. Brown line predicts the biannual maximum surface temperatures, T_{max}, updated from *Paige et al*. [2013]. The grey shaded box corresponds to the area predicted by *Paige et al*. [2013] to have temperatures low enough to sustain water ice on the surface, which also correlates with a clustering of r_s values in the MLA data (Fig. 2f, g).

3.1.3 Small-scale cold trap to the north of crater e5

The third small-scale cold trap identified is located to the north of crater e5, located along a ridge (Fig. 2i; white arrow). The topography of the ridge casts an area of permanent shadow

(Fig. 2l). The PSR correlates with enhanced r_s values as measured by MLA (Fig. 2j) and T_{max} < 100 K capable of sustaining water ice on the surface [*Paige et al*., 2013]. There is a small radar-bright signature that collocates with this small-scale cold trap (Fig. 2l). Overall, the alignment between the permanent shadow, stable freezing temperatures, enhanced r_s values, and radar-bright material are suggestive of exposed water ice within this small-scale cold trap.

The high-reflectance deposit of this small-scale cold trap is in contrast to the large, low-reflectance deposit hosted by crater e5 (Fig. 2j). This low-reflectance deposit, which correlates with radar-bright material (Fig. 2l), is interpreted to insulate subsurface water ice.

3.1.4 Small-scale cold trap in crater l7

Lastly, we identify a flat area on the poleward facing floor of crater l7 (Fig. 2m; white arrow). The MLA data (Fig. 2n, o) show enhanced r_s values, which correlate with T_{max} < 100 K [*Paige et al*., 2013], a PSR, and radar-bright material (Fig. 2p). As with the other three examples, the collocation of these data suggests that water ice is exposed at the surface of this small-scale cold trap.

3.2. Surface reflectance in large craters

Chesterton (88.5°N, 223.1°E), Tolkien (88.8°N, 148.9°E), and Tryggvadóttir (89.6°N, 188.4°E) are the three largest impact craters closest to the north pole of Mercury. We map surface reflectance measurements in all three craters (Fig. 4a, d, g). The number of returns that were strong enough at both the low and high thresholds to enable r_s measurements at these latitudes is much lower than at lower latitudes because of geometric constraints. However, we find a measurable enhancement in the reflectance at the surfaces for each of these craters when compared to the average reflectance of Mercury.

We also map the density of returns for each crater by plotting the probability of detection (Fig. 4b, e, h). For each of the three large craters, there is an increase in the density of returns when crossing into the craters of interest. These density of returns denote that there is an enhancement that is occurring along-track. Given the somewhat sparse coverage of strong MLA energy returns for these craters that permit r_s measurements, these high return densities provide further corroboration that MLA did indeed detect energy enhancements for these craters.

Finally, we calculate the mean r_s value inside each crater, while avoiding crater slopes, and the mean r_s value for the area outside each crater, for areas 2-radii from the crater rim (Fig. 4c, f, i). For each of the large craters, the mean surface reflectance inside the crater exceeded 0.3 and is significantly enhanced relative to the exterior mean r_s values. By including only 75% of the inner crater annulus, we avoid crater slopes in our calculations, thus eliminating the likelihood that these reflectance enhancements could be caused by mass wasting.

We also examined craters that *Neumann et al.* [2013] identified as "MLA-bright" on the basis of data from the MESSENGER primary mission: Prokofiev, Kandinsky, Y, C, A, D2, and i5 (Table S1). We find that all of these craters, except perhaps A and D2, are enhanced relative to the average planetary reflectance (Table S1), consistent with previous findings from limited off-nadir tracks that these craters hosted high-reflectance deposits at the surface composed of water ice [*Neumann et al*., 2013]. In contrast, we find that craters A and D2 have mean r_s values within their PSRs < 0.3 that are not clearly consistent with exposed water-ice deposits on the surface (Table S1).

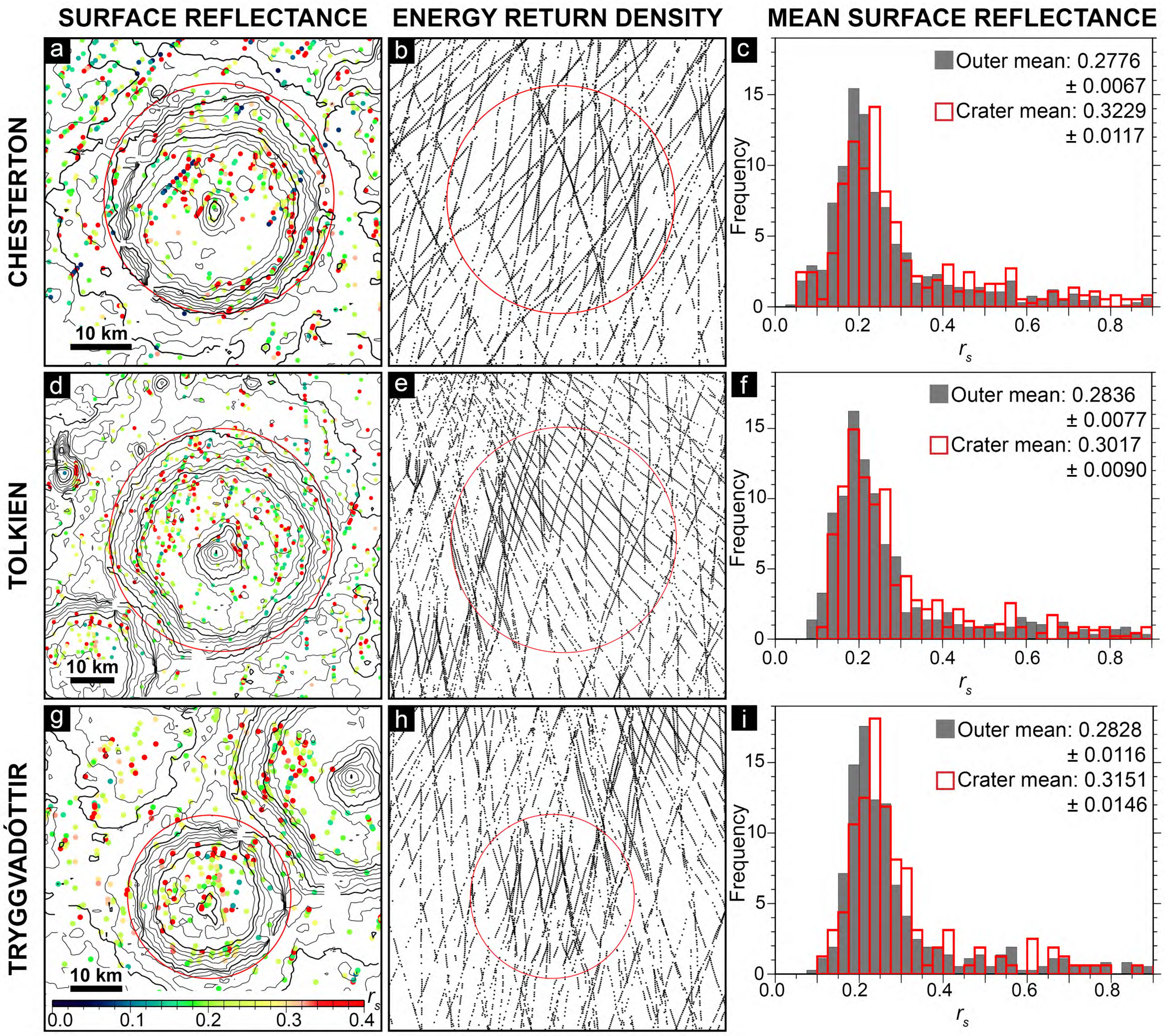

Fig. 4. The first column displays surface reflectance measurements, r_s, for (a) Chesterton (37-km diameter), (d) Tolkien (50-km diameter), and (g), Tryggvadóttir (31-km diameter). Contours are spaced every 200 m. The second column shows the density of energy returns. Crater rim crests outlined in red. The third column shows histograms for surface reflectance, r_s, for the crater (outlined in red) and exterior (shaded in grey) for a 2-radii area, with mean values reported. Each histogram is terminated at $r_s = 0.9$.

4 Discussion

Although we identify only four small-scale cold traps resolvable in the MLA footprints, there are likely to be substantially more micro-cold traps that exist below the spatial resolution of MLA [*Paige et al.*, 2014; *Rubanenko et al.*, 2017]. As discussed in Section 1, maps of the reflectance at the north polar region of Mercury reveal a sharp increase in values northward of ~85°N [*Neumann et al.*, 2017]. The surface reflectance from ~85°N to 90°N is likely to be enhanced by the presence of micro-cold traps that host spatially small water-ice deposits (< a few km in diameter). This interpretation is consistent with the most recent thermal modeling, which suggests that a large fraction of the ice on Mercury resides inside micro-cold traps distributed along the inter-crater terrain, on the scales of 10–100 m rough patches [*Rubanenko et al.*, 2017].

Thermal models [*Paige et al*., 2014] have been used to estimate the total surface area of micro-cold traps in the north polar region of Mercury that are occupied by near-surface water-ice deposits insulated by low-reflectance deposits. However, updated thermal modelling is required for numerical calculations on the percentage of micro-cold traps occupied by exposed water ice. It is reasonable to assume that the fractional area of exposed water ice will increase substantially as well. Thus current estimates of Mercury's water ice inventories are likely to be exceptionally underestimated without accounting for ice within micro-cold traps. For example, conservative modeling suggests that accounting for micro-cold traps on the Moon doubles the cold-trapping area [*Hayne*, 2015].

In our analysis of the mean r_s values inside and outside of the large craters Chesterton, Tolkien, and Tryggvadóttir, the surface reflectances outside of these craters were also enhanced relative to the typical mercurian regolith. The areas outside of these craters (for 2-radii areas) have mean surface reflectances between 0.2776 ± 0.0067 and 0.2836 ± 0.0077, which are values that are enhanced relative to the reflectance of typical mercurian regolith. These regions are not likely to host extensive water-ice deposits due to the low fractional area covered by PSRs and thus the thermal instability of this terrain, but it is possible that the rough terrain close to the pole contains spatially small patches of exposed water ice. These mean values between ~0.25 and 0.3 suggest that there is a mixture of exposed ice (in micro-cold traps) and regolith present (predominantly outside of the cold traps).

5 Conclusions

There is a bimodal distribution of surface reflectance on Mercury in which anomalously low-reflectance deposits correlate with lag deposits insulating water ice and anomalously high-reflectance deposits correlate with exposed water ice. The overall surface reflectance is observed to sharply increase from ~85°N to the pole, even when the presence of large, permanently shadowed craters are removed, suggesting that micro-cold traps may host substantial water ice on the surface of Mercury *[Neumann et al*., 2017]. Here we investigated the possibility that small-scale cold traps could be resolved at the spatial scale of the MLA footprint by searching for clusters of r_s enhancements. We identified four small-scale cold traps that are between 2 and 5 km in diameter (in craters n5, o7, l7, and to the north of e5) on the basis of r_s values exceeding 0.3. These clusters collocated with PSRs and $T_{max} < 100$ K.

We also mapped r_s values for Chesterton, Tolkien, and Tryggvadóttir. Each crater has high radar cross sections indicative of water-ice deposits [*Harmon et al*., 2011], and the derived r_s value for each crater exceeds 0.3, suggesting that water ice is exposed at the surface. The proximity of these three craters to the pole creates a stable thermal environment dominated by temperatures < 100 K in which insufficient sublimation occurs to produce an insulating lag deposit. Thus we identify three new large craters on the surface of Mercury that host extensive water-ice deposits exposed at their surfaces.

Previously, the extent of water-ice deposits was thought to be confined to the extent of large permanently shadowed impact craters and some permanently shadowed rough terrain. However, this conclusion was heavily influenced by the footprint size of the Earth-based observations of the radar-bright material [*Harmon et al*., 2011] and the MESSENGER-derived PSRs [*Chabot et al*., 2012; *Chabot et al.,* 2013; *Deutsch et al*., 2016]. We suggest that large craters are not the only hosts of substantial water-ice deposits on the surface of Mercury, which is consistent with thermal modeling [*Paige et al*., 2014; *Rubanenko et al*., 2017] and reflectance mapping [*Neumann et al*., 2017] results that indicate that micro-cold traps are capable of hosting substantial water-ice deposits. Here we identify four deposits within MESSENGER footprint limits, and suggest that many other deposits exist below the detection limit, within rough patches and inter-crater terrain. We expect that the BepiColombo Laser Altimeter [*Thomas et al*., 2007] will be able to resolve additional high reflectance deposits indicative of surface water ice in mapping the south polar region of Mercury.

Acknowledgments

This work is supported by NASA under Grant Number NNX16AT19H issued through the Harriet G. Jenkins Graduate Fellowship and by the Solar System Exploration Research Virtual Institute. All data analyzed in this paper are available on the NASA Planetary Geodynamics Data Archive (pgda.gsfc.nasa.gov). We thank Andrew Dombard for editorial handling of the manuscript and two anonymous reviewers for insightful reviews.

References

Butler, B. J., D. O. Muhleman, and M. A. Slade (1993), Mercury: full-disk radar images and the detection and stability of ice at the North Pole, *J. Geophys. Res.*, *98*(E8), 15003–15023, doi:10.1029/93JE01581.

Cavanaugh, J. F., J. C. Smith, X. Sun, A. E. Bartels, L. Ramos-Izquierdo, D. J. Krebs, J. F. McGarry, R. Trunzo, A. M. Novo-Gradac, J. L. Britt, J. Karsh, R. B. Katz, A. T. Lukemire, R. Szymkiewicz, D. L. Berry, J. P. Swinski, G. A. Neumann, M. T. Zuber, and D. E. Smith (2007), The Mercury Laser Altimeter Instrument for the MESSENGER Mission, *Space Sci Rev*, *131*(1), 451–479, doi:10.1007/s11214-007-9273-4.

Chabot, N. L., C. M. Ernst, B. W. Denevi, J. K. Harmon, S. L. Murchie, D. T. Blewett, S. C. Solomon, and E. D. Zhong (2012), Areas of permanent shadow in Mercury's south polar region ascertained by MESSENGER orbital imaging, *Geophysical Research Letters*, *39*(9), L09204, doi:10.1029/2012GL051526.

Chabot, N. L., C. M. Ernst, J. K. Harmon, S. L. Murchie, S. C. Solomon, D. T. Blewett, and B. W. Denevi (2013), Craters hosting radar-bright deposits in Mercury's north polar region: Areas of persistent shadow determined from MESSENGER images, *J. Geophys. Res. Planets*, *118*(1), 26–36, doi:10.1029/2012JE004172.

Chabot, N. L., C. M. Ernst, B. W. Denevi, H. Nair, A. N. Deutsch, D. T. Blewett, S. L. Murchie, G. A. Neumann, E. Mazarico, D. A. Paige, J. K. Harmon, J. W., Head, and S. C. Solomon (2014), Images of surface volatiles in Mercury's polar craters acquired by the MESSENGER spacecraft, *Geology*, 1051–1054, doi:10.1130/G35916.1.

Chabot, N. L., E. E. Shread, and J. K. Harmon (2017), Investigating Mercury's south polar water ice deposits, *Lunar Planet. Sci.*, *48*, abstract 1103.

Deutsch, A. N., N. L. Chabot, E. Mazarico, C. M. Ernst, J. W. Head, G. A. Neumann, and S. C. Solomon (2016), Comparison of areas in shadow from imaging and altimetry in the north polar region of Mercury and implications for polar ice deposits, *Icarus*, *280*, 158–171, doi:10.1016/j.icarus.2016.06.015.

Harmon, J. K., and M. A. Slade (1992), Radar Mapping of Mercury: Full-Disk Images and Polar Anomalies, *Science*, *258*(5082), 640–643, doi:10.1126/science.258.5082.640.

Harmon, J. K., M. A. Slade, R. A. Vélez, A. Crespo, M. J. Dryer, and J. M. Johnson (1994), Radar mapping of Mercury's polar anomalies, *Nature*, *369*(6477), 213–215, doi:10.1038/369213a0.

Harmon, J. K., P. J. Perillat, and M. A. Slade (2001), High-Resolution Radar Imaging of Mercury's North Pole, *Icarus*, *149*(1), 1–15, doi:10.1006/icar.2000.6544.

Harmon, J. K., M. A. Slade, and M. S. Rice (2011), Radar imagery of Mercury's putative polar ice: 1999–2005 Arecibo results, *Icarus*, *211*(1), 37–50, doi:10.1016/j.icarus.2010.08.007.

Hayne, P. O. (2015), Effects of small-scale surface topography on volatile distributions on airless bodies, *NASA Exploration Science Forum*, abstract 47.

Lawrence, D. J., W. C. Feldman, J. O. Goldsten, S. Maurice, P. N. Peplowski, B. J. Anderson, D. Bazell, R. L. McNutt, L. R. Nittler, T. H. Prettyman, D. J. Rodgers, S. C. Solomon, and S. Z. Weider (2013), Evidence for Water Ice Near Mercury's North Pole from MESSENGER Neutron Spectrometer Measurements, *Science*, *339*(6117), 292–296, doi:10.1126/science.1229953.

Neumann, G. A., J. F. Cavanaugh, X. Sun, E. Mazarico, D. E. Smith, M. T. Zuber, D. Mao, D. A. Paige, S. C. Solomon, C. M. Ernst, and O. S. Barnouin (2013), Bright and Dark Polar Deposits on Mercury: Evidence for Surface Volatiles, *Science*, *339*(6117), 296–300, doi:10.1126/science.1229764.

Neumann, G. A., A. Sun, E. Mazarico, A. N. Deutsch, J. W. Head, D. A. Paige, L. Rubanenko, and H. C. M. Susorney (2017), Latitudinal variation in Mercury's reflectance from the Mercury Laser Altimeter, *Lunar Planet. Sci.*, *48*, abstract 2660.

Paige, D. A., M. A. Siegler, J. K. Harmon, G. A. Neumann, E. M. Mazarico, D. E. Smith, M. T. Zuber, E. Harju, M. L. Delitsky, and S. C. Solomon (2013), Thermal Stability of Volatiles in the North Polar Region of Mercury, *Science*, *339*(6117), 300–303, doi:10.1126/science.1231106.

Paige, D. A., P. O. Hayne, M. A. Siegler, D. E. Smith, M. T. Zuber, G. A. Neumann, E. M. Mazarico, B. W. Denevi, and S. C. Solomon (2014), Dark surface deposits in the north polar region of Mercury: Evidence for widespread small-scale volatile cold traps, *Lunar Planet. Sci.*, *45*, abstract 2501.

Rubanenko, L., E. Mazarico, G. A. Neumann, and D. A. Paige (2017), Evidence for surface and subsurface ice inside micro cold-traps on Mercury's north pole, *Lunar Planet. Sci.*, *48*, abstract 1461.

Slade, M. A., B. J. Butler, and D. O. Muhleman (1992), Mercury Radar Imaging: Evidence for Polar Ice, *Science*, *258*(5082), 635–640, doi:10.1126/science.258.5082.635.

Sun, X., and G. A. Neumann (2015), Calibration of the Mercury Laser Altimeter on the MESSENGER Spacecraft, IEEE Transactions on Geoscience and Remote Sensing, 53(5), 2860–2874, doi:10.1109/TGRS.2014.2366080.

Thomas, N., T. Spohn, J.-P. Barriot, W. Benz, G. Beutler, U. Christensen, V. Dehant, C. Fallnich, D. Giardini, O. Groussin, K. Gunderson, E. Hauber, M. Hilchenbach, L. Iess, P. Lamy, L.-M. Lara, P. Lognonné, J. J. Lopez-Moreno, H. Michaelis, J. Oberst, D. Resendes, J.-L. Reynaud, R. Rodrigo, S. Sasaki, K. Seiferlin, M. Wieczorek, J. Whitby (2007), The BepiColombo Laser Altimeter (BELA): Concept and baseline design, *Planetary and Space Science*, *55*(10), 1398–1413, doi:10.1016/j.pss.2007.03.003.

Zhang, J. A., and D. A. Paige (2009), Cold-trapped organic compounds at the poles of the Moon and Mercury: Implications for origins, *Geophys. Res. Lett.*, *36*(16), L16203, doi:10.1029/2009GL038614.

Zhang, J. A., and D. A. Paige (2010), Correction to "Cold-trapped organic compounds at the poles of the Moon and Mercury: Implications for origins," *Geophys. Res. Lett.*, *37*(3), L03203, doi:10.1029/2009GL041806.